# Effect of Nonuniform Emission on Miram Curves

David Chernin, Y. Y. Lau, *Fellow, IEEE*, John J. Petillo, *Senior Member, IEEE*, Serguei Ovtchinnikov, Dongzheng Chen, Abhijit Jassem, Ryan Jacobs, Dane Morgan, and John H. Booske, *Fellow, IEEE*

***Abstract*— Analysis of temperature-limited flow, space-charge-limited flow, and the transition between them using a simple planar diode with a thermionic cathode, in which the cathode surface has spatially nonuniform emission properties, is presented. Our theoretical results, which are derived from a model based on solutions to the Vlasov and Poisson equations, compare well with the results of particle-in-cell simulations. We find that the location and the shape of the knee in the anode current versus temperature characteristic (Miram or "rollover" curve) are significantly affected by non-uniformities in the space-charge density in the A–K gap, but are relatively unaffected by the electron motion parallel to the electrode surfaces. In particular, emission from an actively emitting region is strongly affected by the forces (or lack thereof) exerted by the space-charge of the electrons emitted by their neighbors. Perhaps, most remarkably, we find that the limiting current reaching the anode is approximately given by the classical 1-D Child–Langmuir law, even if a significant fraction of the cathode surface is non-emitting.**

***Index Terms*— Cathode, Miram curve, space-charge-limited, temperature-limited, thermionic emission, work function.**

## I. Introduction

THERMIONIC cathodes are widely used as electron sources in electron guns and other devices. As the cathode temperature $T$ is increased, the current reaching the anode transitions from a "temperature-limited" flow, in which all electrons emitted by the cathode reach the anode, to a "space-charge-limited" flow, in which only a small fraction of the emitted electrons make it to the anode, the remainder being returned to the cathode surface. In a simple 1-D model, the temperature-limited current density is given by the Richardson–Dushman (RD) law [1], [2] and the space-charge-limited current density is given by the Child–Langmuir (CL) law [3], [4]. It should be noted that the RD and CL formulas have very different parametric dependencies. In particular, the RD current density depends only on $T$ and $\phi$, the effective average work function of the cathode material, and is independent of the diode geometry and the operating voltage. The CL current density, in distinct contrast, depends only on the diode geometry (A–K gap width) and the operating voltage, and is independent of both $T$ and $\phi$, or any other property of the cathode.

The anode current versus the cathode temperature characteristic of a diode is commonly known as the Miram [5] or "rollover" curve, and the transition from temperature-limited to a space-charge-limited flow is referred to as the "knee" in the curve. As we will show, the transition from a temperature-limited flow to a space-charge-limited flow is very abrupt in a 1-D model, that is, the knee is very sharp. In measurements, however, the transition is generally found to be significantly more gradual than in 1-D theory. We show below that a simple weighted superposition of Miram curves generated by a 1-D model does not predict a smooth knee (as implied, for example, by Gilmour [6, Fig. 5–28]), for the case in which the cathode work function is spatially nonuniform. In fact, it predicts a series of discrete sharp knees, occurring at various temperatures.

The physical reasons behind the shape of Miram (and $I$–$V$) curves have been a mystery for decades, despite the significant efforts made to analyze them, both in experiments and in modeling [5]–[14]. This is an important matter, because a thermionic cathode is almost always operated in the vicinity of the knee in TWTs and klystrons, due to considerations of thermal stability and long-cathode life; gyrotrons, however, are operated below the knee, in the temperature-limited regime.

It is therefore important to understand what processes contribute to the location and the shape of the knee. The major difficulty here is that many complicated factors affect the emission process, including the surface morphology of the cathode, the size and orientations of the cathode grains, the spatial distribution of the work function, local field enhancements due to surface roughness, the velocity distribution of the emitted electrons, and the role of local space-charge effects [5]–[16]. Virtually, none of these has been well characterized for any real cathode. Even the definition of the effective surface area of a cathode is not obvious when, as is often the case, a fraction of the surface is poorly emitting or even non-emitting.

In this article, we isolate one important factor that contributes to the location and the shape of the knee in the Miram curve. Specifically, we show that when the cathode work function is nonuniform, the resulting spatial variation of the space-charge forces has a dramatic effect on the shape of

Manuscript received September 26, 2019; revised November 14, 2019; accepted November 28, 2019. Date of current version January 20, 2020. This work was supported by the Defense Advanced Research Projects Agency (DARPA) under Contract HR0011-16-C-0080. The views, opinions and/or findings expressed are those of the authors and should not be interpreted as representing the official views or policies of the Department of Defense or the U.S. Government. Approved for Public Release, Distribution Unlimited. The review of this article was arranged by Senior Editor C. A. Ekdahl. *(Corresponding author: David Chernin.)*

D. Chernin, J. J. Petillo, and S. Ovtchinnikov are with Leidos Inc., Reston, VA 20190 USA (e-mail: david.p.chernin@leidos.com).

Y. Y. Lau and A. Jassem are with the Department of Nuclear Engineering and Radiological Sciences, University of Michigan, Ann Arbor, MI 48109-2104 USA.

D. Chen, R. Jacobs, and D. Morgan are with the Materials Science and Engineering Department, University of Wisconsin–Madison, Madison, WI 53715-1007 USA.

J. H. Booske is with the Electrical and Computer Engineering Department, University of Wisconsin–Madison, Madison, WI 53715-1007 USA.

Color versions of one or more of the figures in this article are available online at http://ieeexplore.ieee.org.

Digital Object Identifier 10.1109/TPS.2019.2959755

the knee of the Miram curve. In order to illustrate this effect, we formulate and solve a model for the anode current when the cathode is composed of a periodic distribution of "stripes," each having a different value of work function. Our results give some useful insights into the fundamental physics behind Miram curves.

The effects of nonuniform cathode emission have been studied by others [13]–[21], but none of these earlier works explicitly considered the emission mechanism or the details of the transition from temperature-limited to space-charge-limited flow. The results of Umstattd and Luginsland [17], in particular, enable us to interpret several unusual features that we uncover here.

This article is organized as follows: Section II contains a summary of theory that we use to construct Miram curves from the basic equations of emission and electron flow. Section II-A describes a 1-D model, based on the formulation of Fry [22] and Langmuir [4], a useful summary of which may be found in [23]. Section II-B contains our extension of the 1-D model to a case in which the cathode is "tiled" by a periodic arrangement of stripes, each with a different value of work function and/or Richardson "A" coefficient. In this model, we limit the electron motion to 1-D, in the direction normal to the cathode and the anode, but solve Poisson's equation for the potential in 2-D; we refer to this description of the diode as a "$1\frac{1}{2}$-D" model.

We apply the 1-D and $1\frac{1}{2}$-D models to the calculation of Miram curves in Section III. The results of the 1-D model for a cathode with a spatially uniform work function are shown to be in near perfect agreement with those from particle-in-cell simulation using the MICHELLE [24] code. However, a formal application of the 1-D theory to a cathode with spatially varying work function, which treats the configuration as multiple parallel, *non-interacting* diodes, is shown to lead to incorrect results. We then show that the results of the $1\frac{1}{2}$-D model agree very well with MICHELLE simulations for a case in which the cathode is tiled by stripes with alternating values of work function. Using this example, we illustrate how the space-charge above one region affects the current reaching the anode in a neighboring region. Section IV contains a summary and conclusions, and recommendations for future work.

## II. Theory

We consider electron flow in the simple planar diode illustrated in Fig. 1. Electrons are emitted from the cathode located at $z = 0$ and are collected at the anode located at $z = d$. We assign the potential of the cathode to be 0 and that of the anode to be $V_A > 0$. The emission properties (work function and Richardson "$A$" coefficient) of the cathode may depend on $y$, but the cathode temperature and cathode and anode potentials will be assumed to be independent of $y$. We neglect the Schottky effect [25], [6, p. 45] in our model, but mention that this effect is included in the analysis of Zhang *et. al.* [14]. Scott [26] has argued that the Schottky effect may contribute to smoothing of the knee in the $I$–$V$ characteristic curve. However, the Schottky effect is very small compared with the space-charge effects that we study here.

We will further assume that an infinite magnetic field is applied in the $z$-direction. This assumption, which limits the electron motion to the $z$-direction, is not as drastic as it may seem. The results of [17] and our own tests have shown that the Miram curves predicted by particle-in-cell simulations are very nearly independent of the value of the axial magnetic field, that is, nearly independent of the electron motion in the $y$-direction.

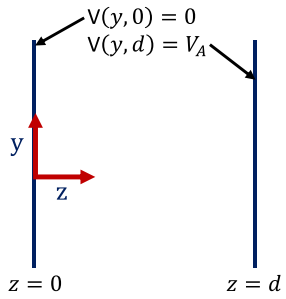


Fig. 1. Simple planar diode.

The electron distribution function, considered as a function of electron position $(y, z)$ and velocity $v_z$, will be assumed to be given by

$$f(y,z;v_z) = f_0(y)e^{-E/kT} = f_0(y)e^{-\left(\frac{1}{2}mv_z^2+qV(y,z)\right)/kT} \quad (1)$$

where $f_0(y)$ is a normalization factor, $E$ is the total energy of an electron, $m$ is the electron mass, $q$ is the electron charge, $k$ is Boltzmann's constant, $T$ is the cathode temperature, and $V(y, z)$ is the electrostatic potential. Since $y$ and $E$ are constants of motion, $f$ is a solution of Vlasov's equation. We assume here that all electron velocities are non-relativistic.

We choose the value of the normalization factor $f_0(y)$ by requiring that the emitted current density be the local RD current density

$$\int_0^\infty dv_z v_z f(y,0;v_z) = J_{\mathrm{RD}}(y) = A(y)T^2e^{-\phi(y)/kT} \quad (2)$$

where $A(y)$ is the local value of the Richardson coefficient and $\phi(y)$ is the local value of work function. Carrying out the elementary integral in (2), we find that

$$f_0(y) = \frac{1}{v_{\mathrm{th}}^2}J_{\mathrm{RD}}(y) \quad (3)$$

wherein we have defined the thermal velocity $v_{\mathrm{th}} \equiv (kT/m)^{1/2}$.

The potential $V(y, z)$ satisfies Poisson's equation

$$\left(\frac{\partial^2}{\partial y^2}+\frac{\partial^2}{\partial z^2}\right)V(y,z) = \left(\frac{\pi}{2}\right)^{1/2}\frac{1}{\epsilon_0 v_{\mathrm{th}}}J_{\mathrm{RD}}(y)e^{-qV(y,z)/kT} * erfc\left(\frac{v_{\mathrm{min}}(y,z)}{2^{1/2}v_{\mathrm{th}}}\right) \quad (4)$$

where $\epsilon_0$ is the permittivity of free space and *erfc* is the complimentary error function. We have obtained the charge density at location $(y, z)$ on the right-hand side of (4) by integrating the distribution function (1) in velocity from the minimum value of velocity $v_{\mathrm{min}}(y, z)$ of any electron that can reach the location $z$ to infinity. Expressions for $v_{\mathrm{min}}(y, z)$ in

terms of local potential $V(y,z)$ may be obtained by applying energy conservation, as shown in Appendix A.

Application of the continuity equation yields the current density at the anode as a function of $y$

$$J_A(y) = J_{\mathrm{RD}}(y)e^{-qV_m(y)/kT}. \tag{5}$$

It is worth noting that the local anode current density $J_A(y)$ depends only on the depth $V_m(y)$ of the potential minimum and not on its location $z_m(y)$.

Of course, we do not know until we solve (4) whether a potential minimum exists or not. It follows that (4) must generally be solved iteratively in order to obtain a self-consistent solution. However, in the special case that all quantities are independent of $y$ (1-D model), Fry [22] and Langmuir [4] have shown how (4) may be solved and an explicit condition obtained for the existence of a potential minimum. We summarize the solution of this 1-D problem below. However, first, we cast our basic equation (4) in a dimensionless form

$$\left(\frac{\partial^2}{\partial \bar{y}^2}+\frac{\partial^2}{\partial \bar{z}^2}\right)\bar{V}(\bar{y},\bar{z}) = 2\bar{J}(y)e^{\bar{V}(\bar{y},\bar{z})} * erfc\left(\frac{\bar{v}_{\min}(\bar{y},\bar{z})}{2^{1/2}}\right) \tag{6}$$

where we have defined the dimensionless quantities

$$\bar{y} \equiv y/d \tag{7a}$$
$$\bar{z} \equiv z/d \tag{7b}$$
$$\bar{V}(\bar{y},\bar{z}) \equiv -qV(y,z)/kT \tag{7c}$$
$$\bar{J}(\bar{y}) \equiv J_{\mathrm{RD}}(y)/J_0 \tag{7d}$$
$$\bar{v}_{\min}(\bar{y},\bar{z}) \equiv v_{\min}(y,z)/v_{\mathrm{th}}. \tag{7e}$$

Here, in (7d), $J_0 \equiv 2(2/\pi)^{1/2}\epsilon_0 v_{\mathrm{th}}^3/((-q/m)d^2) = (9/2\pi^{1/2})J_{\mathrm{CL}}\bar{V}_A^{-3/2}$, where $J_{\mathrm{CL}} = (4\epsilon_0/9d^2)(-2q/m)^{1/2}V_A^{3/2}$ is the classical CL current density.

### A. 1-D Model

Following Fry and Langmuir, we assume that all quantities are independent of $y$. Equation (6) may then be rewritten, following some manipulation, as:

$$\left(\frac{d\eta}{d\xi}\right)^2 = e^{\eta}erfc(\mp\eta^{1/2}) - 1 \mp \frac{2}{\pi^{1/2}}\eta^{1/2} \tag{8}$$

where the upper (lower) signs apply to the $\alpha$- ($\beta$-) region, defined as $0 \le \bar{z} \le \bar{z}_m$ ($\bar{z}_m \le \bar{z} \le 1$), and following Langmuir [4], we have defined:

$$\eta \equiv \bar{V} - \bar{V}_m \tag{9}$$
$$\xi \equiv 2\bar{J}^{1/2}e^{\bar{V}_m/2}(\bar{z}-\bar{z}_m). \tag{10}$$

Equation (8) is equivalent to Langmuir's equation (11). In the relatively uninteresting case, in which no $\alpha$-region exists ($\bar{z}_m = 0$; $\bar{V}_m = 0$), only the lower signs in (8) apply and the anode current is purely temperature-limited, $J_A = J_{\mathrm{RD}}$, that is, all electrons emitted by the cathode reach the anode.

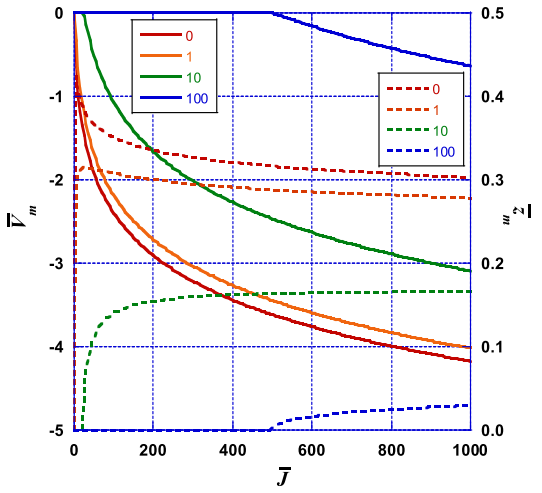


Fig. 2. Normalized value of the minimum potential $\bar{V}_m$ (solid lines, left vertical axis) and its normalized location $\bar{z}_m$ (dashed lines, right axis) versus the normalized current $\bar{J}$ emitted by the cathode for various values of normalized anode voltage $\bar{V}_A$. The values of $\bar{V}_A$ are given in the legends.

Requiring the potential to be continuous at $\bar{z} = \bar{z}_m$ leads to the condition that determines the value of $\bar{V}_m$

$$\int_0^{(-\bar{V}_m)^{1/2}} \frac{udu}{\left[e^{u^2}erfc(-u) - 1 - \frac{2}{\pi^{1/2}}u\right]^{1/2}} + \int_0^{(\bar{V}_A-\bar{V}_m)^{1/2}} \frac{udu}{\left[e^{u^2}erfc(u) - 1 + \frac{2}{\pi^{1/2}}u\right]^{1/2}} = [\bar{J}e^{\bar{V}_m}]^{1/2} \tag{11}$$

where we have defined the normalized voltage at the anode $\bar{V}_A \equiv -qV_A/kT$. The quantity on the right-hand side of (11) is the square root of the anode current density. Once a root of (11) is found for $\bar{V}_m$, the location of the potential minimum is given by

$$\bar{z}_m = [\bar{J}e^{\bar{V}_m}]^{-1/2}\int_0^{(-\bar{V}_m)^{1/2}} \frac{udu}{\left[e^{u^2}erfc(-u) - 1 - \frac{2}{\pi^{1/2}}u\right]^{1/2}}. \tag{12}$$

The values of the normalized electric fields at the cathode and anode surfaces are simply obtained from (8).

Fig. 2 is a plot of $\bar{V}_m$ and $\bar{z}_m$ versus $\bar{J}$ for various values of $\bar{V}_A$, obtained from (11) and (12). Fig. 3 is a plot of the normalized anode current $\bar{J}e^{\bar{V}_m}$ versus $\bar{V}_A$, for various values of $\bar{J}$. The curves in Fig. 3 are the normalized current–voltage characteristics of a 1-D diode.

It follows from (11) that the condition for $\bar{V}_m = 0$, that is, the threshold condition for the formation of a potential minimum, is:

$$\bar{J}_{\mathrm{thr}} = \left[\int_0^{\bar{V}_A^{1/2}} \frac{udu}{\left[e^{u^2}erfc\,(u) - 1 + \frac{2}{\pi^{1/2}}u\right]^{1/2}}\right]^2. \tag{13}$$

Fig. 4 is a plot of $\bar{J}_{\mathrm{thr}}$ versus $\bar{V}_A$. This curve represents the boundary between temperature-limited and space-charge-limited flows (location of the knee) in one dimension. It may

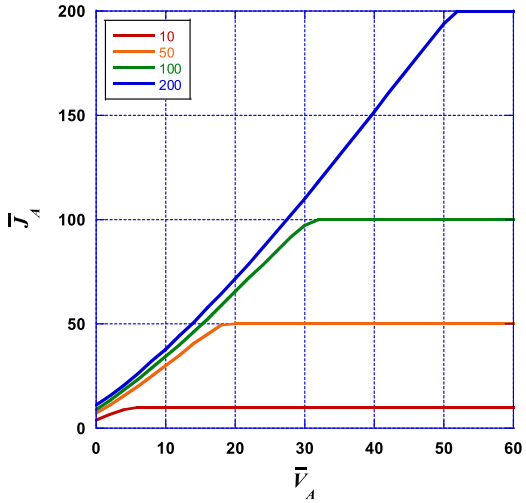


Fig. 3. Normalized anode current $\bar{J}e^{\bar{V}_m}$ versus $\bar{V}_A$, for various values of $\bar{J}$. The values of $\bar{J}$ are given in the legend.

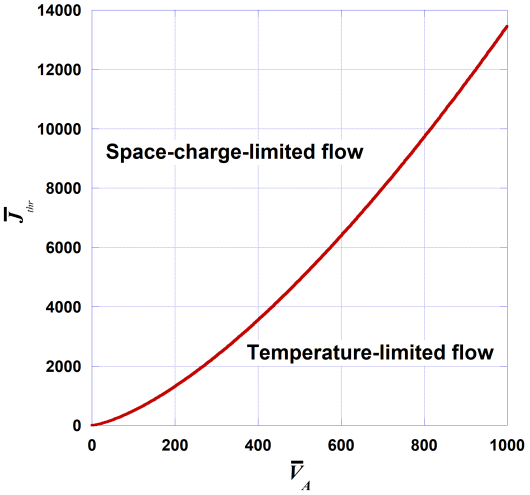


Fig. 4. Normalized threshold emitted current versus $\bar{V}_A$, from (13).

be shown from (13) that $\bar{J}_{\rm thr} \sim (2\pi^{1/2}/9)\bar{V}_A^{3/2} \approx 0.394\bar{V}_A^{3/2}$ for large values of $\bar{V}_A$. In terms of unnormalized quantities, this threshold condition becomes $J_{\rm thr} \sim J_{\rm CL} = J_{\rm RD}$ for large anode voltages.

### *B.* $1\frac{1}{2}$*-D Model*

We return now to consider the solution of (4) and study a particular case in which the cathode properties $A(y)$ and $\phi(y)$ are periodic functions of $y$ with period $p$. A rapidly converging iterative algorithm that we have used successfully to solve a discretized version of (4) is summarized in Appendix B. There, it is shown that the 2-D problem may be reduced to a set of $N_y$-coupled 1-D problems, where $2N_y$ is the number of cells into which a period is divided. Once the potential as a function of $(y, z)$ has been obtained, the depth of the potential minimum $V_m(y_i)$ is known for each $y_i$, where $\{y_i, i = 0, N_y - 1\}$ are the cell centers. The average anode current density may then be computed using

$$J_A = \frac{1}{N_y} \sum_{i=0}^{(N_y-1)} J_{\rm RD}(y_i) e^{-qV_m(y_i)/kT}. \tag{14}$$

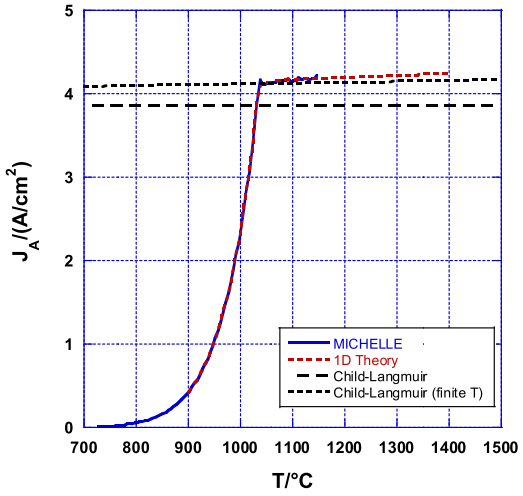


Fig. 5. Miram curve computed using the 1-D theory of Section II-A and by the particle-in-cell simulation code MICHELLE, for a cathode with uniform work function = 2.0 eV. Also shown are the classical CL current density and the classical CL current density, including the finite temperature correction factor of Langmuir.

It is this quantity that is plotted in Figs. 7, 10, and 12 in the next section.

## III. Calculation of Miram Curves

We now apply the 1-D and $1\frac{1}{2}$-D models to the problem of computing the Miram or rollover curves. These curves of anode current versus temperature at a fixed voltage are commonly measured and used to predict the cathode lifetime. In the examples discussed below, we will use diode parameter characteristic of those in a University of Wisconsin test vehicle, $V_A = 179.5$ V and $d = 0.381$ mm. We will take the value of the Richardson "A" coefficient to be the classical value of $1.201732 \times 10^6$ A/(m·°K)$^2$, independent of $y$ for this study.

Fig. 5 shows the Miram curve for a cathode with a spatially uniform work function of 2.0 eV, as computed using the 1-D model of Section II-A, and by the MICHELLE particle-in-cell simulation code [24]. The work function value of 2.0 eV was chosen as a representative of the typical work function of a B-type thermionic dispenser cathode [27]. The agreement between the 1-D model and the MICHELLE simulations is close to perfect, even though no magnetic field was used in the simulations, so the electrons were free to move laterally, parallel to the electrode surfaces. This good agreement also implies that the grid used in the MICHELLE simulations accurately resolves the very small $\alpha$-region between the cathode and the potential minimum.

The space-charge-limited current in Fig. 5 is a slowly increasing function of temperature, a feature that is attributable to the increasing velocity of emission of electrons at the cathode. The value of the classical CL current density, which is derived for zero emission velocity and zero electric field at the cathode, is ~3.867 A/cm$^2$ for the parameters of our problem. This value and the values computed, including the finite temperature correction factor $(1 + 2.66/\bar{V}^{1/2})$ first derived by Langmuir [4] are also shown in Fig. 5.

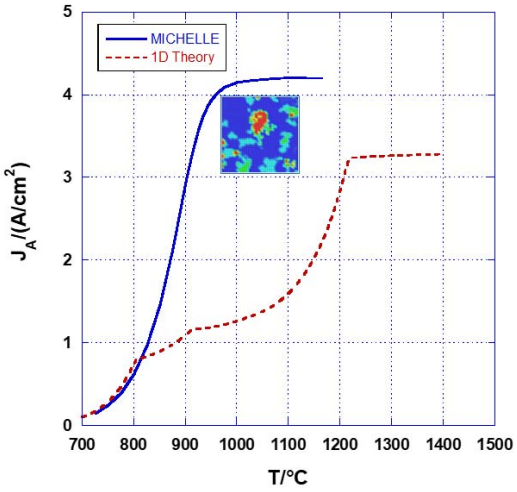


Fig. 6. Miram curves for a cathode with a work function area distribution specified in Table I, as computed by 1-D theory using superposition, and by 3-D MICHELLE simulations. The inset is a cathode surface map of the work function used in the MICHELLE simulations.

TABLE I
WORK FUNCTION AREA DISTRIBUTION

| Work function/eV | Fractional cathode area/% |
|---|---|
| 1.61 | 18.54 |
| 1.79 | 10.32 |
| 2.30 | 10.99 |
| 2.31 | 37.69 |
| Non-emitting | 22.46 |

It might be imagined that in the case of a cathode with a spatially nonuniform work function, the Miram curve may be computed using a weighted superposition of the 1-D model curves, each computed for a single work function; the relative weight of each is chosen to be the area fraction occupied by that work function on the cathode surface. This essentially models the flow as that of independently operating, noninteracting parallel diodes.

As an illustration, we apply this "superposition" approach to the work function distribution given in Table I. This distribution of fractional cathode areas was derived from electron backscatter diffraction measurements made on a tungsten dispenser cathode [16], and the work function values were obtained from density functional theory (DFT) calculations [28]. We note, in particular, the presence of relatively large non-emitting regions, which correspond to pores and other imperfections in the cathode surface [16]. In Fig. 6, we see that the Miram curve computed using the "1-D superposition" approach does not agree with the curve computed by MICHELLE, except at very low temperatures where all parts of the cathode operate as temperature-limited. The MICHELLE simulations were fully 3-D. They used the work function map shown in the inset in Fig. 6, from which Table I was constructed.

We see in Fig. 6 that the space-charge-limited current in the 1-D model is reduced by the fraction (22.46%) of the non-emitting area of the cathode, but the space-charge-limited current computed by MICHELLE is much larger—evidence that emission from the active regions is "making up" for the non-emitting ones. Our conclusion is that the

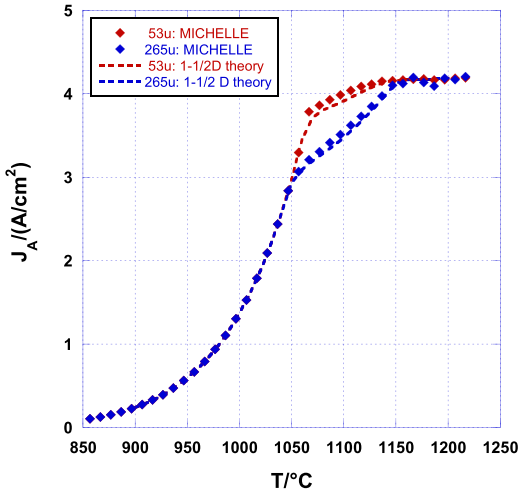


Fig. 7. Miram curves for a cathode with the work function distribution consisting of equal width stripes of alternating work functions (2.0, 2.2) eV, as computed by our $1\frac{1}{2}$-D theory and by MICHELLE.

regions of different work functions *do not emit independently*. Emission from one region is affected, via space-charge fields, by emission (or its absence) from its neighbors.

It is notable that the knee in the MICHELLE curve in Fig. 6 is quite smooth, even though the work function distribution (see Table I) is discrete, unlike the continuous work function distribution assumed in [29]. (Compare the much less smooth knees in the curves in Figs. 7, 10, and 12.) We believe that the smooth transition in Fig. 6 from temperature-limited to space-charge-limited flow may be due to the full 3-D treatment of space-charge, including the lateral motion parallel to the cathode surface, in the MICHELLE simulations.

In order to quantify the influence of emission of one region on another, we apply our $1\frac{1}{2}$-D model to a simple case in which the work function is a periodic function of $y$ of period $p$, consisting of stripes of equal width $p/2$, with alternating, unequal values of work functions $\phi_1$ and $\phi_2$.

Fig. 7 shows the Miram curves from our $1\frac{1}{2}$-D model and from MICHELLE for $\phi_1 = 2.0$ eV, $\phi_2 = 2.2$ eV, for stripe widths $p/2 = 53$ and 265 $\mu$m. The excellent agreement leads us to the conclusion that the interaction between the emitting regions is due to the influence of the space-charge in one region on the emission in other regions. This influence can only be due to changes, caused by the neighboring space charge, in the depth and the location of the local potential minima (as functions of $y$), which strongly affect the amount of emitted current that reaches the anode. We note that the space-charge-limited current is the same for both stripe widths.

We may also conclude that the motion of electrons parallel to the cathode and the anode, which is allowed in MICHELLE, but not in the $1\frac{1}{2}$-D model, is relatively unimportant; no magnetic field is applied in MICHELLE simulations. It is interesting that Adler and Longo [20] found that the motion of electrons parallel to the cathode surface (space-charge smoothing) contributes to the fact that the limiting current is determined by the CL law, when the work function is nonuniform. Here, we find that even in the case where no motion parallel to the electrode surfaces is allowed, the limiting

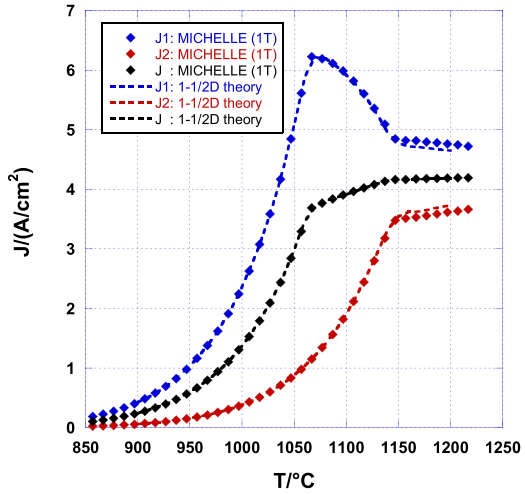


Fig. 8. Contributions to the total anode current from regions of different work functions, for the case of Fig. 7, for stripe width = 53 $\mu$m. *J1* (blue) is the current density at the anode opposite the low (2.0 eV) work function region on the cathode; *J2* (red) is the current density opposite the high (2.2 eV) work function region, and $J = (J1 + J2)/2$ (black) is the average anode current density. The MICHELLE simulations included an axial magnetic field of 1 T.

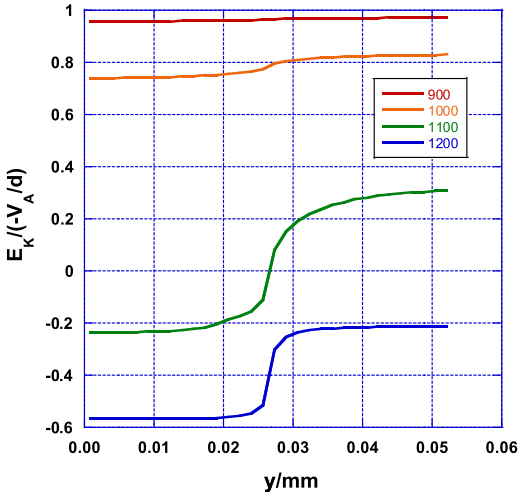


Fig. 9. Normalized electric field at the cathode surface as a function of $y$ for various temperatures, for the case of Fig. 7, for stripe width = 0.0530 mm. The 2.0-eV work function region extends from $y = 0$ to 0.0265 mm; the 2.2-eV work function region extends from 0.0265 to 0.0530 mm. The values in the legend specify the cathode temperature in °C.

current is still determined by the CL law. The unimportance of lateral motion was also noted in [17] and [21].

Finally, we note that the computational time required by the $1\frac{1}{2}$-D model code to compute the anode current at each temperature was on the order of 0.3 s on a desktop PC, while the corresponding MICHELLE simulations required a few seconds to a few minutes, depending on the temperature and on the total particle count and other numerical parameters.

It is interesting to examine the contributions to the total anode current from the regions of different work functions as a function of temperature. Fig. 8 illustrates the results from the $1\frac{1}{2}$-D model (dashed lines) and MICHELLE simulations[1] (points) for $p/2 = 53\mu$m. We see the remarkable rollover of the contribution from the lower work function region (*J1*), as a function of temperature. We attribute this rollover to the effect of the space-charge emitted by its neighbor, the higher work function region, i.e., as the current produced by the *higher* work function region increases with temperature, its space-charge starts to affect the depth and the location of the potential minimum in front of the cathode in the *lower* work function region. This is a purely 2-D effect, completely absent in the 1-D theory of Section II-A.

Fig. 8 may be qualitatively understood as follows. It was shown in [18] and [21], by considering the 2-D space-charge effects, that the anode current density due to emission from a stripe of finite width $w$ may exceed the classical 1-D CL value by a factor of approximately $(1 + (d/\pi w))$, where $d$ is the anode–cathode spacing. At moderately low temperatures, when *J2* is much smaller than *J1*, the effective value of $w$ is just the width of a single stripe. However, as the temperature is increased and *J2* becomes significant, the effective value of $w$ increases, which reduces the factor by which the current density may exceed the CL value. This implies that *J1* must eventually rollover as *J2* increases, consistent with Fig. 8. The average of *J1* and *J2*, which we denote as *J* in Fig. 8, monotonically approaches the CL value.

Fig. 9 is a plot of the normal electric field at the cathode surface versus $y$ for various temperatures. We see that as the temperature is increased, the normal electric field is reversed first over the low work function region and then over the high work function region. A reversed electric field at the cathode surface, of course, signifies the existence of a potential minimum in front of the cathode.

Next, in order to more fully explore the insensitivity of the limiting current to the presence of non-emitting regions, we use our two stripe model with $\phi_1 = 2.1$ eV and $\phi_2 = 10.0$ eV, i.e., one stripe is emitting and the second stripe is not, in the temperature range of interest. We fix the total width $p = 20$ $\mu$m, but vary the relative width of the non-emitting region from zero percent to 95 percent of the full period. The resulting average anode current density is shown in Fig. 10, which again shows excellent agreement between the $1\frac{1}{2}$-D model (solid curves) and MICHELLE simulations (dashed curves) for all cases. It is striking that even with 40% of the cathode non-emitting (third curve from left in Fig. 10), essentially the same Miram curve was obtained as an 100%-emitting cathode (leftmost curve in Fig. 10), except for a shift of about 40 °C for the onset of space-charge-limited emission. The average anode current tends toward the same value at high temperatures, regardless of the fraction of the non-emitting area. This shows that at sufficiently high temperatures, emission from the active regions is indeed making up for the lack of emission from the inactive regions, as our comparison of MICHELLE simulations with 1-D analysis (see Fig. 6) suggested. Umstattd and Luginsland [17] first discovered this remarkable 2-D effect; they did not, however,

[1]The MICHELLE simulations of Fig. 8 used an axial magnetic field $B_z =$ 1T in order to confine the electron motion predominately to the $\hat{z}$-direction. When a smaller magnetic field (or no magnetic field) is used, the *J1* and *J2* curves of Fig. 8 are shifted slightly up and down, respectively, but in such a way that the $J = (J1 + J2)/2$ (Miram) curve is, to a remarkable degree, unchanged, that is, we find that the Miram curve is very insensitive to the value of $B_z$.

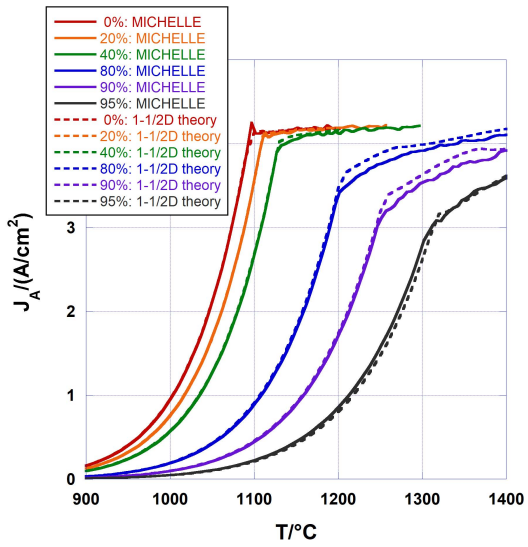


Fig. 10. Average anode current density versus $T$ for alternating values of work function (2.1 eV [emitting] and 10.0 eV [non-emitting]) for different stripe widths, computed using our $1\frac{1}{2}$-D model ($B_z = \infty$), solid curves, and MICHELLE ($B_z = 0$), dashed curves. The legend specifies the percentage of the total width that is non-emitting.

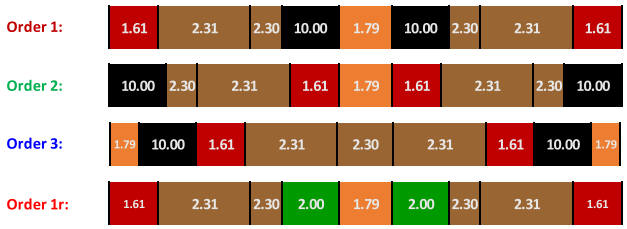


Fig. 11. Various orderings of eight stripes with different work functions; the two end half-stripes are considered as one because of the periodicity condition. Work function values in volts are shown in white. Stripe widths are proportional to the measured area fractions. Total width = 1 period = 80 $\mu$m.

consider the detailed physical mechanism or the transition from temperature-limited to space-charge-limited flow.

Finally, we consider a more complicated case, illustrated in Fig. 11, in which the work function period contains eight stripes. The values of the work functions are from experimentally determined values listed in Table I. The width of each stripe is taken to be proportional to its fractional occurrence in the distribution. The average stripe width is taken to be 10 $\mu$m, which is a typical scale size for a tungsten surface grain, so the full period $p = 80$ $\mu$m. An important feature of data in Table I is the existence of a significant non-emitting region ($\sim$22% of the entire cathode in this case), to which we again assign a work function value of 10 eV in our model calculations.

We consider various "orderings" of the eight stripes within a period, as illustrated in Fig. 11. Fig. 12 shows the resulting Miram curves computed with the $1\frac{1}{2}$-D model. We see that the shape of the transition ("knee region") from temperature-limited to space-charge-limited flow depends on the ordering of the stripes, but the saturated, space-charge-limited current is the same for all orderings. Figs. 11 and 12 include a case "Order 1r" in which the non-emitting regions in "Order 1" are replaced by emitting regions with $\phi = 2$ eV. As expected from our earlier results, the space-charge-limited current is

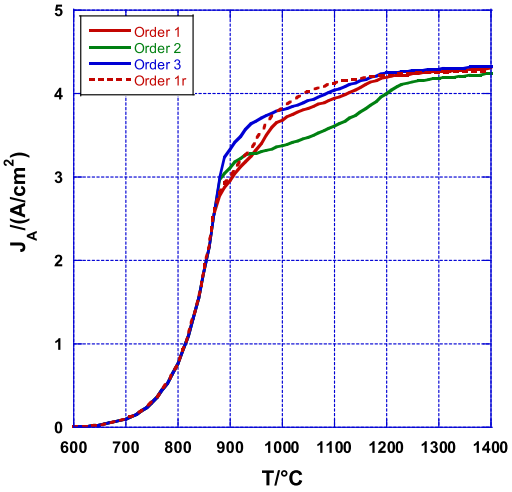


Fig. 12. Miram curves computed using $1\frac{1}{2}$-D theory, for various stripe orderings illustrated in Fig. 11.

unchanged, even though non-emitting regions of the cathode have been replaced by emitting ones. We conclude that the space-charge-limited current is again accurately given by the classical CL formula (including Langmuir's finite temperature correction; see Fig. 5).

## IV. Summary and Conclusion

We have generalized the 1-D diode model of Fry and Langmuir to include the effects of microscopic variations in the cathode emission properties. We have assumed that the electron motion is confined to one direction only, but have allowed the space-charge fields to vary in two dimensions. We have used the new model to compute Miram curves for various distributions of work function on the cathode surface. We have found that the shape of the Miram curve near the knee is significantly affected by the work function distribution, but the space-charge-limited current density is still accurately given by the classical CL law in all cases examined, including cases in which significant portions of the cathode are non-emitting. We have found that the electron motion parallel to the cathode surface has little effect on the shape of the Miram curves.

While our numerical studies were restricted to a diode with $V_A = 179.5$ V, $d = 0.381$ mm, we expect that the general features revealed would occur generally in diodes with other voltages and gap widths because of the very wide ranges of operating regimes that we have studied, viz., nonmagnetized and highly magnetized electron flow, low-fraction and high-fraction active emitting regions, 1-D and 2-D analytic theory and comparison with MICHELLE simulations, interacting and non-interacting stripes and uniform, systematic, and highly random work function distributions, both in 1-D and 2-D.

Our study corroborates the general notion that the shape of the Miram curve depends on the cathode material properties, which may change with age. We have now moved a step further, demonstrating quantitatively how the effects of nonuniform emission from the cathode surface strongly affect the shape of the curves. We speculate that local electric

field enhancements due to cathode surface roughness, which was neglected in this article, will exert a similar influence by contributing additional emission non-uniformities on an otherwise flat cathode surface. If confirmed by further studies, this observation could lead to substantial simplification of the simulation of electron emission from rough surfaces.

It would be straightforward to include $y$-dependence of the cathode temperature and potential and the Schottky effect [25] in the numerical algorithm summarized in Appendix B.

Future work may include the generalization of the $1\frac{1}{2}$-D model to $2\frac{1}{2}$-D, in which the cathode work function is tiled in both the $x$- and $y$-directions, but with electron motion still restricted to the $z$-direction. Such a model could be used to generate predictions of Miram curves that may be directly compared with experimental measurements. It may also shed additional light on the origins of the smooth transition between temperature-limited and space-charge-limited flows noted in the 3-D simulation results shown in Fig. 6.

Finally, we note that the problem inverse to the one studied here, that is, the determination of the work function distribution from the Miram (or $I$–$V$) curves [5], [11], [13], [14], [29] is much more difficult than computing the Miram curve directly from a specified work function distribution, as is done in this article. The work on the inverse problem appears to have been limited to inferring properties (e.g., standard deviations) of the spatially integrated work function distribution. The results illustrated in Fig. 12 demonstrate that the shape of the Miram curve in the transition region depends on the detailed spatial distribution of the work function. We consequently suggest that it may be possible to infer (some properties of) the spatial distribution from the form of the Miram curves, though this is highly speculative.

## Appendix A
## Expressions for $v_{\min}$

First, we consider the case in which the potential encountered by an electron as it moves away from the cathode toward the anode is a monotonically increasing function of $z$, that is, the minimum in the potential as a function of $z$ is $V_m(y) = 0$, which occurs at the cathode surface, $z = 0$. In this case, $v_{\min}(y, z)$ is the velocity at $z$ of a particle that was emitted from the cathode with zero velocity, from which it follows from the conservation of total (kinetic + potential) energy that

$$v_{\min;0}(y,z) = \left(\frac{-2qV(y,z)}{m}\right)^{1/2}. \tag{A1}$$

Next, we consider what happens when there is a potential minimum $V_m(y) < 0$ occurring at $z = z_m > 0$. In this case, only electrons emitted from the cathode with velocity greater than $(2qV_m(y)/m)^{1/2}$ will make it over the potential hill and reach the anode, while the others will be returned to the cathode. It follows that for $0 < z < z_m$ ($\alpha$–region)

$$v_{\min;\alpha}(y,z) = -\left(\frac{-2q(V(y,z) - V_m(y))}{m}\right)^{1/2} \tag{A2}$$

and for $z_m < z < d$ ($\beta$–region)

$$v_{\min;\beta}(y,z) = +\left(\frac{-2q(V(y,z) - V_m(y))}{m}\right)^{1/2}. \tag{A3}$$

## Appendix B
## Numerical Algorithm for the Solution of (4)

We summarize an algorithm for the numerical solution of (4), in the case $V(y+p, z) = V(y, z)$, for a specified period $p$, and $V(-y, z) = V(y, z)$; the latter condition applies to all of the examples in the text.

We write (4) as

$$\nabla^2 V(y,z) = S[y;V] \tag{B1}$$

where we have defined the right-hand side of (4) as the source term $S$, which is a nonlinear function of $y$ and $V$. Equation (B1) may be solved iteratively, as follows.

We define $N_y$, discrete, "cell centered" values of $y$ as

$$y_i \equiv \frac{i + 1/2}{N_y}(p/2) \tag{B2}$$

for $i = 0, 1, \ldots N_y - 1$ and express the potential at these points as a Fourier series

$$V_i(z) = \frac{2}{N_y} {\sum_{k=0}^{(N_y-1)}}' \tilde{V}_k(z) \cos\left(\frac{2\pi k}{p} y_i\right) \tag{B3}$$

where the prime mark on the sum means that the $k = 0$ term has an additional factor of $1/2$. If we discretize the second derivative with respect to $y$ in (B1), we find that $\tilde{V}_k(z)$ satisfies

$$\frac{d^2}{dz^2}\tilde{V}_k - \frac{2}{(\Delta y)^2}(1 - \cos\theta_k)\tilde{V}_k = \tilde{S}_k \tag{B4}$$

for $k = 0, 1, \ldots N_y - 1$, where $\theta_k \equiv \pi k/N_y$, $\Delta y \equiv p/(2N_y)$ is the cell size in $y$, and $\tilde{S}_k$ is the discrete Fourier transform of $S$ given by

$$\tilde{S}_k = \sum_{i=0}^{(N_y-1)} S_i \cos\left(\frac{2\pi k}{p} y_i\right). \tag{B5}$$

We require the boundary conditions[2] on $\tilde{V}_k(z)$ to be

$$\tilde{V}_k(0) = 0;\ k = 0, 1, \ldots N_y - 1 \tag{B6a}$$

$$\tilde{V}_k(d) = \begin{cases} N_y V_A; & k = 0 \\ 0; & k > 0. \end{cases} \tag{B6b}$$

Suppose that now we have an approximate solution on the discrete $y$-grid for the potential, which we denote as $V_i^{(n)}(z)$, where the superscript $(n)$ denotes the $n$th approximation in our iterative solution. The next approximation is obtained as follows:

1) Evaluate $S[y; V^{(n)}]$. This step requires that we examine $V_i^{(n)}(z)$ as a function of $z$ for each $i$ and determine the location of the potential minimum, if one exists. Referring to (4) in the text, we observe from (A2) and (A3) that the form of $S[y; V^{(n)}]$ is different on either side of the potential minimum.
2) Compute the Fourier coefficients of $S[y; V^{(n)}(y, z)]$ using (B5). This may be done very quickly using a fast Fourier transform when $N_y$ is an integer power of 2.
3) Solve the set of equations (B4), subject to the boundary conditions (B6a) and (B6b). This may be done, for

[2]A different boundary condition could be applied at $z = 0$ to account for the differences in potential of cathode regions with different work functions.

example, by the widely used Thomas algorithm [30], [31] for tri-diagonal systems on a grid in $z$.

4) Construct a new potential, which we denote as $V_i^{(n+)}$, using (B3).
5) The $(n+1)$ approximation to the potential is then

$$V_i^{(n+1)} = \alpha V_i^{(n)} + (1-\alpha) V_i^{(n+)} \tag{B7}$$

where the mixing parameter $\alpha$ is a real number satisfying $0 < \alpha < 1$. The choice of $\alpha$ must be made empirically, in order to obtain convergence. Near the knee in the Miram curve, for example, we have found that $\alpha \gtrsim 0.8$ may be required.

The iteration must be started with an initial guess for $V(y, z)$. A reasonable choice is the vacuum solution $V_A(z/d)$, though other choices can lead to faster convergence.

Using this algorithm, we have found that on the order of 10–100 iterations using $\alpha = 0.9$ are typically required in order to obtain convergence of the potential everywhere to one part in $10^4$.

## REFERENCES


[1] O. W. Richardson, *The Emission of Electricity from Hot Bodies*. London, U.K.: Longmans, Green, and Company, 1916.

[2] S. Dushman, "Electron emission from metals as a function of temperature," *Phys. Rev.*, vol. 21, no. 6, pp. 623–636, 1923, doi: 10.1103/PhysRev.21.623.

[3] C. Child, "Discharge from hot CaO," *Phys. Rev. (Ser. I)*, vol. 32, p. 492, May 1911, doi: 10.1103/PhysRevSeriesI.32.492.

[4] I. Langmuir, "The effect of space charge and initial velocities on the potential distribution and thermionic current between parallel plates," *Phys. Rev.*, vol. 21, no. 4, p. 419, Apr. 1923, doi: 10.1103/PhysRev.21.419.

[5] M. J. Cattelino, G. V. Miram, and W. R. Ayers, "A diagnostic technique for evaluation of cathode emission performance and defects in vehicle assembly," in *IEDM Tech. Dig.*, San Francisco, CA, USA, Dec. 1982, pp. 36–39, doi: 10.1109/IEDM.1982.190205.

[6] A. S. Gilmour, Jr., *Klystrons, Traveling Wave Tubes, Magnetrons, Crossed-Field Amplifiers, and Gyrotrons*. Boston, MA, USA: Artech House, 2011.

[7] K. Jensen, *Introduction to the Physics of Electron Emission*. Hoboken, NJ, USA: Wiley, 2017.

[8] R. T. Longo, "A study of thermionic emitters in the regime of practical operation," in *IEDM Tech. Dig.*, Washington, DC, USA, Dec. 1980, pp. 467–470, doi: 10.1109/IEDM.1980.189868.

[9] R. Vaughan, "A synthesis of the Longo and Eng cathode emission models," *IEEE Trans. Electron Devices*, vol. ED-33, no. 11, pp. 1925–1927, Nov. 1986, doi: 10.1109/T-ED.1986.22844.

[10] T. J. Grant, "Emission degradation characteristics of coated dispenser cathodes," in *IEDM Tech. Dig.*, Los Angeles, CA, USA, Dec. 1986, pp. 700–703, doi: 10.1109/IEDM.1986.191289.

[11] M. Cattelino and G. Miram, "Predicting cathode life expectancy and emissino quality from PWFD measurements," *Appl. Surf. Sci.*, vol. 111, pp. 90–95, Feb. 1997, doi: 10.1016/S0169-4332(96)00718-0.

[12] G. Miram, L. Ives, M. Read, R. Wilcox, M. Cattelino, and B. Stockwell, "Emission spread in thermionic cathodes," in *Proc. 5th IEEE IVEC*, Apr. 2004, pp. 303–304, doi: 10.1109/IVELEC.2004.1316330.

[13] S. P. Khodnevich, "Determination of emission homogeneity on the cathode by current-voltage characteristic," *Electron. Technol., Microw. Electron.*, vol. 20, no. 4, pp. 118–130, 1969.

[14] J. Zhang, S. Illy, I. Gr. Pagonakis, T. Rzesnicki, A. Avramidis, A. Malygin, S. Ruess, A. Samartsev, G. Dammertz, B. Piosczyk, G. Gantenbein, M. Thumm and J. Jelonnek, "Evaluation and influence of gyrotron cathode emission inhomogeneity," *IEEE Trans. Electron Devices*, vol. 64, no. 3, pp. 1307–1314, Mar. 2017, doi: 10.1109/TED.2017.2655147.

[15] P. Zhang, A. Valfells, L. K. Ang, J. W. Luginsland, and Y. Y. Lau, "100 years of the physics of diodes," *Appl. Phys. Rev.*, vol. 4, Mar. 2017, Art. no. 011304, doi: 10.1063/1.4978231.

[16] D. Chen, R. Jacobs, V. Vlahos, D. Morgan, and J. Booske, "Statistical model of non-uniform emission/rom polycrystalline tungsten cathodes," in *Proc. Int. Vac. Electron. Conf. (IVEC)*, Busan, South Korea, May 2019, pp. 1–2, doi: 10.1109/IVEC.2019.8745051.

[17] R. Umstattd and J. Luginsland, "Two dimensional space charge limited emission: Beam edge characteristics and applications," *Phys. Rev. Lett.*, vol. 87, Mar. 2001, Art. no. 145002, doi: 10.1103/PhysRevLett.87.145002.

[18] Y. Y. Lau, "Simple theory for the two-dimensional Child-Langmuir law," *Phys. Rev. Lett.*, vol. 87, no. 27, 2001, Art. no. 278301, doi: 10.1103/PhysRevLett.87.278301.

[19] J. W. Luginsland, Y. Y. Lau, R. J. Umstattd, and J. J. Watrous, "Beyond the Child-Langmuir law: A review of recent results on multidimensional space-charge-limited flow," *Phys. Plasmas*, vol. 9, no. 5, p. 2371, Apr. 2002, doi: 10.1063/1.1459453.

[20] E. A. Adler and R. T. Longo, "Effect of nonuniform work function on space-charge-limited current," *J. Appl. Phys.*, vol. 59, no. 4, pp. 1022–1027, 1986, doi: 10.1063/1.336535.

[21] J. W. Luginsland, Y. Y. Lau, and R. M. Gilgenbach, "Two-dimensional Child-Langmuir law," *Phys. Rev. Lett.*, vol. 77, no. 22, pp. 4668–4670, 1996, doi: 10.1103/PhysRevLett.77.4668.

[22] T. Fry, "The thermionic current between parallel plane electrodes; velocities of emission distributed according to Maxwell's law," *Phys. Rev.*, vol. 17, no. 4, p. 441, Apr. 1921, doi: 10.1103/PhysRev.17.441.

[23] C. Quate, "Shot noise from thermionic cathodes," in *Noise in Electron Devices*, L. D. Smullin and H. A. Haus, Eds. Cambridge, MA, USA: MIT Press, 1959, pp. 1–44.

[24] J. Petillo, E. M. Nelson, J. F. DeFord, N. J. Dionne, and B. Levush, "Recent advances in the MICHELLE 2D/3D electron gun and collector modeling code," *IEEE Trans. Electron Devices*, vol. 52, no. 5, pp. 742–748, May 2005, doi: 10.1109/TED.2005.845800.

[25] W. Schottky, "Über den Einfluss von Strukturwirkungen, besonders der Thomsonschen Bildkraft, auf die Elektronenemission der Metalle (On the influence of structural effects, especially Thomson's image force, on the electron emission of metals)," *Physik Zeitschr.*, vol. 15, pp. 872–878, 1914.

[26] J. B. Scott, "Extension of Langmuir space-charge theory into the accelerating field range," *J. Appl. Phys.*, vol. 52, no. 7, pp. 4406–4410, Jul. 1981, doi: 10.1063/1.329367.

[27] R. Forman, "A proposed physical model for the impregnated tungsten cathode based on Auger surface studies of the Ba-O-W system," *Appl. Surf. Sci.*, vol. 2, no. 2, p. 258, 1979.

[28] R. Jacobs, J. Booske, and D. Morgan, "Work function and surface stability of tungsten-based thermionic electron emission cathodes," *Appl. Mater.*, vol. 5, no. 11, Nov. 2017, Art. no. 116105, doi: 10.1063/1.5006029.

[29] J. C. Tonnerre, D. Brion, P. Palluel, and A. M. Shroff, "Evaluation of the work function distribution of impregnated cathodes," *Appl. Surf. Sci.*, vol. 16, nos. 1–2, pp. 238–249, 1983 (http://dx.doi.org/10.1016/0378-5963(83)90070-3).

[30] L. H. Thomas, *Elliptic Problems in Linear Difference Equations Over a Network*. New York, NY, USA: Columbia Univ., 1949.

[31] S. D. Conte and C. de Boor, *Elementary Numerical Analysis*. Philadelphia, PA, USA: SIAM, 2018, pp. 153–156.


**David Chernin** received the Ph.D. degree in applied mathematics from Harvard University, Cambridge, MA, USA, in 1976.

He is currently a Senior Staff Scientist with Leidos Inc., Reston, VA, USA. Since 1984, he has been with Leidos Inc., and its predecessor company SAIC, where he has conducted research on beam-wave interactions and other topics in the physics of particle accelerators and vacuum electron devices.

**Y. Y. Lau** (M'98–SM'06–F'07) received the B.S., M.S., and Ph.D. degrees in electrical engineering from the Massachusetts Institute of Technology, Cambridge, MA, USA, in 1968, 1970, and 1973, respectively.

He is currently a Professor with the University of Michigan, Ann Arbor, MI, USA, where he is specialized in RF sources, heating, and discharge.

Dr. Lau was elected Fellow of the American Physical Society (APS) in 1986. He received the 1999 IEEE Plasma Science and Applications Award and the 2017 IEEE John R. Pierce Award for Excellence in Vacuum Electronics. He served three terms as an Associate Editor for *Physics of Plasmas* from 1994 to 2002.

**John J. Petillo** (M'99–SM'12) received the B.S. degree in electrical engineering from Northeastern University, Boston, MA, USA, in 1980, and the Ph.D. degree in applied plasma physics from the Massachusetts Institute of Technology, Cambridge, MA, USA, in 1986. His dissertation was on equilibrium and stability analysis of the modified betatron accelerator.

He has been with Leidos Inc., Reston, VA, USA, formerly (Science Applications International Corporation/SAIC), since 1986, first in McLean, VA, USA, and currently in Billerica, MA, USA. Since joining Leidos/SAIC, he has been involved in the research and development of analysis software and analysis and advanced modeling and simulation of RF components, including vacuum electronics, emission physics, accelerator components, microwave devices, ion beam lithography, and ion thrusters. He has been a Lecturer with the U.S. Particle Accelerator School on several occasions in the area of beam and EM-PIC field modeling. He is currently the Director of the Center for Electromagnetic Science, Leidos Innovation Center (LInC), Leidos Inc., and also the Research and Development Manager and an author of the MICHELLE, MASK, AVGUN, and ARGUS Codes.

**Serguei Ovtchinnikov** received the B.S. degree in physics and mathematics and the M.S. and Ph.D. degrees in computer science (numerical analysis) from the University of Colorado at Boulder, Boulder, CO, USA, in 1995, 2001, and 2006, respectively.

He is currently a Senior Staff Scientist at Leidos Inc., Billerica, MA, USA. His research interests focus on applications of High Performance Computing (HPC) to computational electromagnetics.

**Dongzheng Chen** received the B.S. degree in physics from Peking University, Beijing, China, in 2016, and the M.S. degree in materials science and engineering from the University of Wisconsin–Madison, Madison, WI, USA, in 2017, where he is currently pursuing the Ph.D. degree with the Department of Materials Science and Engineering.

His current research interests include thermionic emission modeling and space-charge effects.

**Abhijit Jassem** received the B.S. degree in nuclear engineering from Purdue University, West Lafayette, IN, USA, in 2016. He is currently pursuing the Ph.D. degree with the University of Michigan's Nuclear Engineering and Radiological Sciences Program, University of Michigan, Ann Arbor, MI, USA.

He is working with the Plasma, Pulsed Power, and Microwave Laboratory, University of Michigan, Ann Arbor, MI, USA, under the supervision of Prof. Y. Y. Lau.

**Ryan Jacobs** received the B.S. degree in materials science and engineering from the University of Minnesota-Twin Cities, Minneapolis, MN, USA, in 2010, the M.S. and Ph. D. degrees in materials science from the University of Wisconsin–Madison, Madison, WI, USA, in 2012 and 2015, respectively.

He is currently a Research Scientist with the Department of Materials Science and Engineering, University of Wisconsin–Madison. His work focuses on using atomistic modeling and machine learning to understand the structure and properties of materials at the atomic scale, with a particular focus on the discovery and engineering of novel material compounds for specific technological applications. His main research application areas of interest comprise materials for energy technology, such as solid oxide fuel cells, lithium ion batteries, and solar photovoltaics, with another main thrust of his research centered around investigating the surface electronic and thermodynamic properties of metals and oxides used as electron emission cathodes.

**Dane Morgan** received the Ph.D. degree in physics from the University of California at Berkeley, Berkeley, CA, USA, in 1998.

He was a Post-Doctoral Researcher and a Research Scientist with the Massachusetts Institute of Technology (MIT) until 2004. He is currently a Professor in materials science and engineering with the University of Wisconsin–Madison, Madison, WI, USA. His work combines thermostatistics, thermokinetics, and informatics analysis with atomic scale calculations to understand and predict materials properties. He is presently training or has graduated/trained over 60 graduate students and post-doctoral researchers and worked with approximately 150 undergraduates in research. He is also the Harvey D. Spangler Professor of engineering and a University of Wisconsin Vilas Scholar, where he received multiple teaching and research awards and has published over 250 articles in materials science.

**John H. Booske** (S'82–M'85–SM'93–F'07) is currently a Vilas Distinguished Achievement Professor with the Electrical and Computer Engineering Department, University of Wisconsin–Madison, Madison, WI, USA. His research interests include experimental and theoretical study of coherent electromagnetic radiation, its sources and its applications, spanning the RF, microwave, millimeter-wave, and THz regimes.

Dr. Booske is a fellow of the American Physical Society in 2011. He received the IEEE EAB Major Educational Innovation Award in 2014 and the IEEE Plasma Science and Applications Award in 2018.